

# Topological Charge Quadrupole Protected by Spin-Orbit $U(1)$ Quasi-Symmetry in Antiferromagnet NdBiPt

Ao Zhang<sup>1,\*</sup>, Xiaobing Chen<sup>2,1,\*</sup>, Jiayu Li<sup>1</sup>, Pengfei Liu<sup>1</sup>, Yuntian Liu<sup>1</sup> and Qihang Liu<sup>1,3,4,†</sup>

<sup>1</sup>*Department of Physics and Shenzhen Institute for Quantum Science and Engineering (SIQSE), Southern University of Science and Technology, Shenzhen 518055, China*

<sup>2</sup>*Quantum Science Center of Guangdong–Hong Kong–Macao Greater Bay Area (Guangdong), Shenzhen 518045, China*

<sup>3</sup>*Guangdong Provincial Key Laboratory for Computational Science and Material Design, Southern University of Science and Technology, Shenzhen 518055, China*

<sup>4</sup>*Shenzhen Key Laboratory of Advanced Quantum Functional Materials and Devices, Southern University of Science and Technology, Shenzhen 518055, China*

\*These authors contributed equally to this work.

†Email: [liuqh@sustech.edu.cn](mailto:liuqh@sustech.edu.cn)

## Abstract

The interplay of symmetry and topology in crystal solids has given rise to various elementary excitations as quasiparticles. Among these, those with significant Berry-phase-related transport responses are of particular interest. Here, we predict a new type of quasiparticle called topological charge quadruple (TCQ), which is analogous to a charge quadrupole but consists of two closely-packed pairs of Weyl points in momentum space, specifically in a half-Heusler antiferromagnet NdBiPt. Interestingly, the TCQ is protected by the spin-orbit  $U(1)$  quasi-symmetry, rather than any exact crystallographic symmetries. This quasi-symmetry restricts the energy splitting induced by symmetry-lowering perturbations to a second-order effect. Furthermore, the closely located Berry curvature sources and sinks in the TCQ lead to a large Berry curvature dipole, resulting in a significant nonlinear Hall effect. Our work opens an avenue for designing novel quasiparticles using quasi-symmetries and developing materials with enhanced nonlinear responses.

## Introduction

The investigation of topological semimetals and the discovery of gapless elementary excitations in these materials have been a prosperous area of research in condensed matter physics (1-4). Various types of emergent quasiparticles, exemplified by Dirac (5-10), Weyl (11-19), and new fermions beyond them (20-23), have been predicted and observed in solids as low-energy fermionic excitations near the band crossings protected by symmetry and topology. The discovery of these quasiparticles has also led to the use of crystallographic symmetry-based language, i.e., space groups and magnetic space groups, to classify topological materials (24-32). Recently, the classification of quasiparticles was extended to spin space groups to treat magnetic materials with negligible spin-orbit coupling, predicting various types of multifold band degeneracies and unconventional quasiparticles in both electronic and magnonic spectra (33-38). The topological semimetals of particular interest are those hosting quasiparticles with observable transport responses. One such example is that magnetic Weyl semimetals exhibit the linear and nonlinear anomalous Hall effect (39-41) induced by Berry curvature. In contrast, Dirac semimetals, protected by  $PT$ -symmetry (where  $P$  and  $T$  denote space inversion and time reversal, respectively), exhibit a vanishing Berry curvature throughout momentum space and no related transport effects (Fig. 1A). Therefore, a long-sought goal is to identify ideal materials with topological quasiparticles being close to the Fermi level and exhibiting significant transport properties.

In this work, we propose a new type of quasiparticle, dubbed topological charge quadrupole (TCQ), in a noncentrosymmetric half-Heusler compound NdBiPt with a collinear antiferromagnetic (AFM) order. Analogous to the charge quadrupole, the TCQ consists of four Weyl points in momentum space that are closely located, with two having a topological charge of +1 and the other two having a topological charge of -1, as shown in Fig. 1B. Interestingly, such a quasiparticle complex is not protected by exact symmetry but rather by a novel spin-orbit  $U(1)$  quasi-symmetry (42, 43). While the electronic structure of NdBiPt closely resembles a Dirac semimetal, the four nearly degenerate Weyl points manifest Berry curvature sources and sinks within a small region of momentum space, leading to strong Berry curvature dipole (BCD) and nonlinear Hall effects (Fig. 1B). The TCQ of NdBiPt results in a significant BCD peak located only 5.8 meV below the Fermi level, and the peak value is comparable to those of the  $T_d$  phase of  $WTe_2$  (44) and collinear AFM CuMnSb (41). Furthermore, the strong dependence of the

BCD on the Néel vector can be used for the detection of the Néel vector. Our work not only reveals the important role of hidden symmetry in predicting new quasiparticles, but also provides a new approach for designing significant quantum geometric effects in unconventional AFM materials.

### Topological charge quadrupole in NdBiPt

Recent neutron diffraction measurements show that NdBiPt accommodates an A-type collinear AFM configuration (45) along the [001] direction of the nonmagnetic cubic conventional cell below the Néel temperature  $T_N = 2.18 K$ , resulting in the tetragonal magnetic unit cell with lattice constants  $a = b = 4.78 \text{ \AA}$  and  $c = 6.76 \text{ \AA}$  (Fig. 2A). The magnetic geometry and the SOC-free electronic structure are fully described by its spin space group  $G_S = P\bar{4}1m^{12-1}(1/2\ 1/2\ 1/2)^{\infty m}1$  (No. 115.119.2.1) (46, 47). Especially, the collinear magnetic order is described by the spin-only group  $G_{SO} = {}^{\infty m}1 = SO(2) \rtimes Z_2^K$  (only contains pure spin operations), where  $SO(2)$  and  $Z_2^K$  represent the continuous spin rotations along the collinear spin axis and the mirror symmetry  $TU$  in spin space ( $U$  is the twofold rotation along any axis perpendicular to the collinear spin axis), respectively (see Supplementary S2 for detailed symmetry analysis). The DFT-calculated band structure without SOC is shown in Fig. 2C (see Supplementary S1 for computational methods). Two prominent features are observed. The first one is the double degeneracy throughout the whole Brillouin zone protected by the  $U\tau$  and  $SO(2)$  symmetries (38, 46), where  $\tau = (1/2, 1/2, 1/2)$  is the fractional translation symmetry that connects the two opposite-spin sublattices. Notably,  $U\tau$ -enforced double degeneracy provides new quasiparticles with doubled topological charges from two  $P$ -broken spin channels (36, 37), which differs from compensated ones enforced by  $PT$  symmetry (38). Secondly, a four-fold degenerate  $\beta$  band (orange line) intersects with a two-fold degenerate  $\alpha$  band (green line), forming a six-fold degenerate quasiparticle at the  $Q(0, 0, 0.006\frac{2\pi}{c})$  point. Such a  $\beta$  band comprises a Dirac nodal line along  $-Q - \Gamma - Q$ , as shown in Fig. 2D, while the nodal line splits off this high-symmetry line (fig. S2.1).

Since NdBiPt is composed of heavy elements, the corresponding electronic structure with SOC is expected to exhibit significant SOC-induced band splitting as shown in Fig. 2E. The electronic structure with SOC is dictated by its magnetic space group  $G_M = P\bar{4}n2$  (No. 118.314). In the presence of SOC, both  $U\tau$  and  $SO(2)$  symmetries are broken, leading to the spin-polarized

non-degenerate bands. However, the bands along the  $\Gamma - Z$  direction maintain twofold degeneracy, which is protected by two-fold rotation  $\{2_{001}|0\}$  and glide mirror  $\{m_{010}|\tau\}$  (see Supplementary S2). Additionally, the fourfold degenerate  $\beta$  band splits into  $\beta_1$  and  $\beta_2$ . Surprisingly, while the SOC gap between  $\alpha$  and  $\beta_2$  ( $\Delta E_{\alpha\beta_2}$ ) at the  $Q$  point remarkably reaches 672.4 meV (indicated by the black arrow), an unexpectedly small SOC gap  $\Delta E_{\alpha\beta_1} = 9.2$  meV emerges between  $\alpha$  and  $\beta_1$ . To illustrate the evolution of the SOC effect, we present the electronic structures with varying SOC strength  $\lambda$  in fig. S2.2. Specifically, as  $\lambda$  increases,  $\Delta E_{\alpha\beta_2}$  exhibits a significant linear increase from 0 to 672.4 meV, while  $\Delta E_{\alpha\beta_1}$  increases gradually and eventually reaches 9.2 meV (Fig. 2F). The substantial difference between  $\Delta E_{\alpha\beta_1}$  and  $\Delta E_{\alpha\beta_2}$  cannot be explained by traditional group representation theory because  $\alpha$ ,  $\beta_1$ , and  $\beta_2$  bands share the same two-dimensional irreducible representation  $\bar{Q}_5$  of the little group  $G_M^Q = \bar{4}'m2'$  at the  $Q$  point.

We next look into the fine electronic structure within the tiny gap of  $\Delta E_{\alpha\beta_1}$ , where multiple Weyl points reside. In the noncentrosymmetric  $T\tau$ -AFM NdBiPt, each Weyl point has a  $T\tau$  partner of the same chirality. Meanwhile, two glide mirror symmetries,  $\{m_{100}|\tau\}$  and  $\{m_{010}|\tau\}$ , connect Weyl points of opposite chirality. Consequently, an AFM Weyl semimetal with eight Weyl nodes is confirmed by DFT calculations, as shown in Fig. 3A. Taking a close look off the  $Q$  point, we have uncovered two pairs of Weyl points with charge  $\pm 1$  (fig. S2.3). Due to the tiny gap at  $Q$ , these Weyl points form a square with a side length of  $0.01\text{\AA}^{-1}$ , which is only 1/131 of the in-plane reciprocal lattice parameter. Therefore, such a closely packed configuration of Weyl points forms a topological charge quadrupole (TCQ) in momentum space. Because of the  $T\{2_{001}|\tau\}$  symmetry, the chirality distribution around  $Q$  and  $-Q$  points are the same, as shown in Fig. 3A. Therefore, in the (001) surface Brillouin zone, the Weyl points are projected pairwise on four different projected positions  $W_i$  ( $i = 1, 2, 3, 4$ ) with an effective topological charge of  $\pm 2$ . Such a distribution of Weyl points results in two overlapping Fermi rings composed of four individual Fermi arcs, and further forms two closed Fermi rings due to band hybridization (see the right panel of Fig. 3A). We calculate the Fermi arc surface states on the (001) surface, where the two closed Fermi ring surface states are presented in Fig. 3B. The smaller Fermi ring connecting the TCQ is further shown in Fig. 3C.

## Spin-orbit $U(1)$ quasi-symmetry

The key feature of the TCQ is the near degenerate Weyl points, which cannot be well explained by any exact symmetries. However, recent studies showed that the classical group representation theory can be extended to address the issue of near degeneracy by using the concept of quasi-symmetry (42, 43, 48). In general, quasi-symmetry refers to the hidden symmetry within a degenerate orbital subspace under an unperturbed Hamiltonian  $H^0$  and limits the occurrence of the symmetry-lowering term, denoted as  $H'$ , to only second-order effects. While the previous studies focused on nonmagnetic systems, we next demonstrate that the formation of the TCQ in AFM NdBiPt can be attributed to a new type of spin-orbit  $U(1)$  quasi-symmetry. Such a symmetry results in the partially lifted band degeneracy under the first-order SOC effect, and thus a tiny gap when involving the second-order SOC effect at the  $Q$  point.

By analyzing the DFT-calculated orbital projection of the bands along the  $\Gamma - Z$  direction (figs. S2.4-S2.6 and table S2.2), we can effectively write the  $\alpha$ ,  $\beta_1$ , and  $\beta_2$  bands as:

$$\begin{cases} \alpha = (|l_0, \uparrow\rangle + |l_0, \downarrow\rangle)/\sqrt{2} \\ \beta_1 = (|l_+, \uparrow\rangle + |l_-, \downarrow\rangle)/\sqrt{2} \\ \beta_2 = (|l_-, \uparrow\rangle + |l_+, \downarrow\rangle)/\sqrt{2} \end{cases} \quad (1)$$

where  $l_0$  and  $l_{\pm}$  can be expressed as linear combinations of the atomic orbitals, designated as  $|l_0\rangle = \theta|s\rangle + \gamma|p_z\rangle$  and  $|l_{\pm}\rangle = \frac{1}{\sqrt{2}}(|u_x\rangle \pm i|u_y\rangle)$ , where  $|u_{x/y}\rangle = \eta|p_{x/y}\rangle + \delta|d_{xz/yz}\rangle$ . In the absence of SOC, the symmetry of the Hamiltonian  $H_A^0 = H_k + H_p + H_{mag}$ , which includes the kinetic term  $H_k$ , the potential term  $H_p$  and the magnetic term  $H_{mag}$ , can be described by  $G_{H_A^0} = G_S$ . The doubly degenerate band  $\alpha$  and the four-fold degenerate band  $\beta$  with irreps  $Q_{1,A}^{1/2}(2)$  and  $Q_{3,A}^{1/2}Q_{4,A}^{1/2}(4)$  of the little group  $G_{H_A^0}^Q = m\bar{4}1m^m2^{\infty}21$  intersect at the  $Q$  point as shown in Fig. 4A. When including SOC,  $\beta$  band splits into two doubly degenerate bands  $\beta_1$  and  $\beta_2$ . The band crossing between  $\alpha$  and  $\beta_1$  is gapped (and so is that between  $\alpha$  and  $\beta_2$ ), because  $\alpha$ ,  $\beta_1$ , and  $\beta_2$  bands share the same magnetic group representation  $\bar{Q}_5(2)$  (Fig. 4D). We next use the quasi-symmetry theory to elucidate the remarkable difference of two SOC-induced gaps at the  $Q$  point,  $\Delta E_{\alpha\beta_1}$ , and  $\Delta E_{\alpha\beta_2}$ .

Note that the difference between  $\Delta E_{\alpha\beta_1}$  and  $\Delta E_{\alpha\beta_2}$  cannot be captured using any group extended by  $G_{H_A^0}^Q$ , which failed in separating bands  $\beta_1$  and  $\beta_2$  (see Supplementary S3.1). Interestingly, we find that the  $\lambda L_z S_z$  term does not contribute to the two SOC gaps but splits the  $\beta$  band into bands  $\beta_1$  and  $\beta_2$  (see Supplementary S3.2). Therefore, we consider the unperturbed Hamiltonian  $H_B^0 = H_A^0 + \lambda L_z S_z$  and the perturbed Hamiltonian  $H_B' = \frac{\lambda}{2}(L_+ S_- + L_- S_+)$ . The introduction of  $\lambda L_z S_z$  breaks the little group  $G_{H_A^0}^Q$  into  $G_{H_B^0}^Q = \bar{1}\bar{4}^2 m^m 2^\infty 1$ , thus providing an adequate starting point of three doubly degenerate bands (Fig. 4B). Then we find that the spin-orbit  $U(1)$  symmetry  $P_q = \{U_z(\theta) \| R_z(\theta)\}$  (49, 50), which represents the simultaneously continuous rotation along the  $z$ -direction in both spin and lattice space, is not in  $G_{H_B^0}^Q$ , but commutes with  $H_B^0$  and  $H_B'$ . It transforms the matrix element  $\langle \alpha | H_B' | \beta_1 \rangle$  into an additional phase factor, i.e.,  $\langle \alpha | H_B' | \beta_1 \rangle \xrightarrow{P_q} e^{i\omega(P_q)} \langle \alpha | H_B' | \beta_1 \rangle$ , thereby enforcing the first-order SOC effect between  $\alpha$  and  $\beta_1$  bands to be zero (43). In contrast, two elements of  $\langle \alpha | H_B' | \beta_2 \rangle$  are transformed as an identity representation (see Supplementary S3.3), resulting in a relatively larger gap as shown in Fig. 4C. Consequently, the first-order SOC-induced gap at  $Q$  is zero between  $\alpha$  and  $\beta_1$  bands, leading to a small second-order gap of 9.2 meV. In contrast, the band crossing of  $\alpha$  and  $\beta_2$  bands is lifted by first-order SOC with 672.4 meV (Fig. 4D).

To validate the above quasi-symmetry analysis, we constructed a  $k \cdot p$  model near the  $\Gamma$  point (see Supplementary S4). The distinction between two SOC gaps can be estimated utilizing the first-order SOC Hamiltonian  $H_{soc}^{(1)} = \lambda L \cdot S$  (See Eq. S4.3),

$$\Delta E_{\alpha\beta_1}^{(1)} \sim \langle \alpha | H_{soc}^{(1)} | \beta_1 \rangle = \lambda/2(h_{15} + h_{25} + h_{16} + h_{26}) = 0 \quad (2)$$

$$\Delta E_{\alpha\beta_2}^{(1)} \sim \langle \alpha | H_{soc}^{(1)} | \beta_2 \rangle = \lambda/2(h_{13} + h_{23} + h_{14} + h_{24}) = \sqrt{2}\lambda/2. \quad (3)$$

Eqs. (2) and (3) show that the first-order SOC effect is prohibited for  $\Delta E_{\alpha\beta_1}$  but is allowed for  $\Delta E_{\alpha\beta_2}$ , consistent with the framework of quasi-symmetry analysis. Therefore, we demonstrate that the TCQ, two closely-packed pairs of Weyl points within the tiny gap at the  $Q$  point, is protected by spin-orbit  $U(1)$  quasi-symmetry.

## Large nonlinear Hall effect

The TCQ gathers the sources and sinks of Berry curvature in a very small region in momentum space, leading to a remarkable BCD. Thus, an enhanced nonlinear Hall effect is expected if the TCQ emerges around the Fermi level, as shown in Fig. 1B. In  $T\tau$ -AFM NdBiPt, there is only one independent element  $D_{xy} = D_{yx}$  of the BCD tensor  $\mathbf{D}$  (see Eq. S2.2), where  $D_{xy} = \int_{BZ} dk \sum_n f_0(\varepsilon_{nk}) \left( \frac{\partial}{\partial k_x} \Omega_y \right)$ . The distribution of the Berry curvature  $\Omega_y$  on the  $k_x - k_y$  plane is shown in Fig. 4E. We find that  $\Omega_y$  is mainly concentrated near the TCQ. Due to the presence of two glide mirrors  $\{m_{100}|\tau\}$  and  $\{m_{010}|\tau\}$ ,  $\Omega_y$  is antisymmetric along the  $k_x$  direction and symmetric along the  $k_y$  direction. The gapped  $Q$  point (black triangles in Fig. 4E) is located between the peaks of the positive and negative Berry curvature around the TCQ. Furthermore, the distribution of  $\Omega_y$  in the vicinity of the Fermi surface is non-uniform due to the tilting of the Weyl cones. Overall, such a distribution pattern of the Berry curvature gives rise to a large BCD (see figs. S2.7-S2.8).

The BCD density  $d_{xy}$  along the high-symmetry paths is shown in Fig. 4F, indicating that the origin of  $d_{xy}$  comes entirely from the contribution of the TCQ around the  $Q$  point. Since the BCD is the integral of  $d_{xy}$ , it is consistent with our calculation of BCD exhibiting a peak at the position of the TCQ, as shown in Fig. 4G. The large BCD value approaches 0.02 when the chemical potential is located at the TCQ (the black dashed line in Fig. 4G). This value is comparable to the previous study on CuMnSb (41), while the BCD peak for CuMnSb is located at about 100 meV above the Fermi level. In comparison, thanks to the clean Fermi surface composed of the TCQ, the BCD peak of NdBiPt is located only 5.8 meV below the Fermi level, which is favorable for experimental detection.

In summary, based on the spin group analysis, we extend the quasi-symmetry theory to elucidate the formation of a new type of quasiparticle TCQ, which is the analogy of charge quadrupole but composed of two closely-packed pairs of Weyl points in momentum space. Our DFT calculations show that the noncentrosymmetric half-Heusler compound NdBiPt with a collinear AFM configuration is an ideal material candidate, manifesting a clean Fermi surface with TCQ. The structure of TCQ is protected by the mirror symmetry and more importantly, the spin-orbit  $U(1)$  quasi-symmetry that eliminates the first-order SOC gap, leading to a significant

nonlinear Hall effect induced by BCD. Overall, our research provides an avenue for the design of novel quasiparticles by quasi-symmetries and the design of material candidates with large nonlinear physical responses. Furthermore, the exotic transport properties induced by TCQ can also be used for the detection of the Néel vector, providing more possibilities for antiferromagnetic spintronics.

## Acknowledgments

This work was supported by the National Key R&D Program of China under Grant No. 2020YFA0308900, the National Natural Science Foundation of China under Grant No. 12274194, Guangdong Provincial Key Laboratory for Computational Science and Material Design under Grant No. 2019B030301001, Shenzhen Science and Technology Program (Grants No. RCJC20221008092722009 and No. 20231117091158001), the Science, Technology and Innovation Commission of Shenzhen Municipality (Grant No. ZDSYS20190902092905285) and Center for Computational Science and Engineering of Southern University of Science and Technology.

## References

1. C.-K. Chiu, J. C. Y. Teo, A. P. Schnyder, S. Ryu, Classification of topological quantum matter with symmetries. *Rev. Mod. Phys.* **88**, 035005 (2016).
2. B. Yan, C. Felser, Topological Materials: Weyl Semimetals. *Annu. Rev. Condens. Matter Phys.* **8**, 337-354 (2017).
3. N. P. Armitage, E. J. Mele, A. Vishwanath, Weyl and Dirac semimetals in three-dimensional solids. *Rev. Mod. Phys.* **90**, 015001 (2018).
4. B. Q. Lv, T. Qian, H. Ding, Experimental perspective on three-dimensional topological semimetals. *Rev. Mod. Phys.* **93**, 025002 (2021).
5. Z. Wang *et al.*, Dirac semimetal and topological phase transitions in  $A_3\text{Bi}$  ( $A=\text{Na, K, Rb}$ ). *Phys. Rev. B* **85**, 195320 (2012).
6. S. M. Young *et al.*, Dirac Semimetal in Three Dimensions. *Phys. Rev. Lett.* **108**, 140405 (2012).



7. Z. Wang, H. Weng, Q. Wu, X. Dai, Z. Fang, Three-dimensional Dirac semimetal and quantum transport in Cd<sub>3</sub>As<sub>2</sub>. *Phys. Rev. B* **88**, 125427 (2013).
8. Z. K. Liu *et al.*, A stable three-dimensional topological Dirac semimetal Cd<sub>3</sub>As<sub>2</sub>. *Nat. Mater.* **13**, 677-681 (2014).
9. Z. K. Liu *et al.*, Discovery of a Three-Dimensional Topological Dirac Semimetal, Na<sub>3</sub>Bi. *Science* **343**, 864-867 (2014).
10. S.-Y. Xu *et al.*, Observation of Fermi arc surface states in a topological metal. *Science* **347**, 294-298 (2015).
11. X. Wan, A. M. Turner, A. Vishwanath, S. Y. Savrasov, Topological semimetal and Fermi-arc surface states in the electronic structure of pyrochlore iridates. *Phys. Rev. B* **83**, 205101 (2011).
12. H. Weng, C. Fang, Z. Fang, B. A. Bernevig, X. Dai, Weyl Semimetal Phase in Noncentrosymmetric Transition-Metal Monophosphides. *Phys. Rev. X* **5**, 011029 (2015).
13. S.-M. Huang *et al.*, A Weyl Fermion semimetal with surface Fermi arcs in the transition metal monpnictide TaAs class. *Nat. Commun.* **6**, 7373 (2015).
14. S.-Y. Xu *et al.*, Discovery of a Weyl fermion semimetal and topological Fermi arcs. *Science* **349**, 613-617 (2015).
15. B. Q. Lv *et al.*, Experimental Discovery of Weyl Semimetal TaAs. *Phys. Rev. X* **5**, 031013 (2015).
16. L. X. Yang *et al.*, Weyl semimetal phase in the non-centrosymmetric compound TaAs. *Nat. Phys.* **11**, 728-732 (2015).
17. B. Q. Lv *et al.*, Observation of Weyl nodes in TaAs. *Nat. Phys.* **11**, 724-727 (2015).
18. Y. Sun, S.-C. Wu, B. Yan, Topological surface states and Fermi arcs of the noncentrosymmetric Weyl semimetals TaAs, TaP, NbAs, and NbP. *Phys. Rev. B* **92**, 115428 (2015).
19. Z. K. Liu *et al.*, Evolution of the Fermi surface of Weyl semimetals in the transition metal pnictide family. *Nat. Mater.* **15**, 27-31 (2016).
20. B. Bradlyn *et al.*, Beyond Dirac and Weyl fermions: Unconventional quasiparticles in conventional crystals. *Science* **353**, aaf5037 (2016).
21. B. Q. Lv *et al.*, Observation of three-component fermions in the topological semimetal molybdenum phosphide. *Nature* **546**, 627-631 (2017).

22. J. Z. Ma *et al.*, Three-component fermions with surface Fermi arcs in tungsten carbide. *Nat. Phys.* **14**, 349-354 (2018).
23. Z.-M. Yu *et al.*, Encyclopedia of emergent particles in three-dimensional crystals. *Sci. Bull.* **67**, 375-380 (2022).
24. J. Kruthoff, J. de Boer, J. van Wezel, C. L. Kane, R.-J. Slager, Topological Classification of Crystalline Insulators through Band Structure Combinatorics. *Phys. Rev. X* **7**, 041069 (2017).
25. H. Watanabe, H. C. Po, A. Vishwanath, Structure and topology of band structures in the 1651 magnetic space groups. *Sci. Adv.* **4**, eaat8685 (2018).
26. T. Zhang *et al.*, Catalogue of topological electronic materials. *Nature* **566**, 475-479 (2019).
27. F. Tang, H. C. Po, A. Vishwanath, X. Wan, Comprehensive search for topological materials using symmetry indicators. *Nature* **566**, 486-489 (2019).
28. M. G. Vergniory *et al.*, A complete catalogue of high-quality topological materials. *Nature* **566**, 480-485 (2019).
29. Y. Xu *et al.*, High-throughput calculations of magnetic topological materials. *Nature* **586**, 702-707 (2020).
30. A. Bouhon, G. F. Lange, R.-J. Slager, Topological correspondence between magnetic space group representations and subdimensions. *Phys. Rev. B* **103**, 245127 (2021).
31. L. Elcoro *et al.*, Magnetic topological quantum chemistry. *Nat. Commun.* **12**, 5965 (2021).
32. B. Peng, Y. Jiang, Z. Fang, H. Weng, C. Fang, Topological classification and diagnosis in magnetically ordered electronic materials. *Phys. Rev. B* **105**, 235138 (2022).
33. J. Yang, Z.-X. Liu, C. Fang, Symmetry invariants and classes of quasi-particles in magnetically ordered systems having weak spin-orbit coupling. *arXiv:2105.12738*, (2021).
34. P.-J. Guo, Y.-W. Wei, K. Liu, Z.-X. Liu, Z.-Y. Lu, Eightfold Degenerate Fermions in Two Dimensions. *Phys. Rev. Lett.* **127**, 176401 (2021).
35. P. Liu, J. Li, J. Han, X. Wan, Q. Liu, Spin-Group Symmetry in Magnetic Materials with Negligible Spin-Orbit Coupling. *Phys. Rev. X* **12**, 021016 (2022).
36. P. Liu, A. Zhang, J. Han, Q. Liu, Chiral Dirac-like fermion in spin-orbit-free antiferromagnetic semimetals. *The Innovation* **3**, 100343 (2022).
37. A. Zhang *et al.*, Chiral Dirac fermion in a collinear antiferromagnet. *Chin. Phys. Lett.* **40**, 126101 (2023).

38. X. Chen, J. Ren, J. Li, Y. Liu, Q. Liu, Spin space group theory and unconventional magnons in collinear magnets. *arXiv:2307.12366*, (2023).
39. E. Liu *et al.*, Giant anomalous Hall effect in a ferromagnetic kagome-lattice semimetal. *Nat. Phys.* **14**, 1125-1131 (2018).
40. Q. Wang *et al.*, Large intrinsic anomalous Hall effect in half-metallic ferromagnet  $\text{Co}_3\text{Sn}_2\text{S}_2$  with magnetic Weyl fermions. *Nat. Commun.* **9**, 3681 (2018).
41. D. Shao, S. Zhang, G. Gurung, W. Yang, E. Y. Tsybal, Nonlinear Anomalous Hall Effect for Néel Vector Detection. *Phys. Rev. Lett.* **124**, 067203 (2020).
42. C. Guo *et al.*, Quasi-symmetry-protected topology in a semi-metal. *Nat. Phys.* **18**, 813-818 (2022).
43. J. Li, A. Zhang, Y. Liu, Q. Liu, Group Theory on Quasisymmetry and Protected Near Degeneracy. *Phys. Rev. Lett.* **133**, 026402 (2024).
44. J.-S. You, S. Fang, S.-Y. Xu, E. Kaxiras, T. Low, Berry curvature dipole current in the transition metal dichalcogenides family. *Phys. Rev. B* **98**, 121109 (2018).
45. R. A. Müller *et al.*, Magnetic structure of the antiferromagnetic half-Heusler compound  $\text{NdBiPt}$ . *Phys. Rev. B* **92**, 184432 (2015).
46. X. Chen *et al.*, Enumeration and Representation Theory of Spin Space Groups. *Phys. Rev. X* **14**, 031038 (2024).
47. See <https://findspingroup.com> for the online program *FINDSPINGROUP* of spin-space-group identification and the spin space group for collinear antiferromagnet  $\text{NdBiPt}$ .
48. L. Liu, Y. Liu, J. Li, H. Wu, Q. Liu, Quantum spin Hall effect protected by spin  $U(1)$  quasi-symmetry. *arXiv:2402.13974*, (2024).
49. F. Sun, J. Ye, W.-M. Liu, Quantum magnetism of spinor bosons in optical lattices with synthetic non-Abelian gauge fields. *Phys. Rev. A* **92**, 043609 (2015).
50. J. Y. Lee *et al.*, Theory of correlated insulating behaviour and spin-triplet superconductivity in twisted double bilayer graphene. *Nat. Commun.* **10**, 5333 (2019).

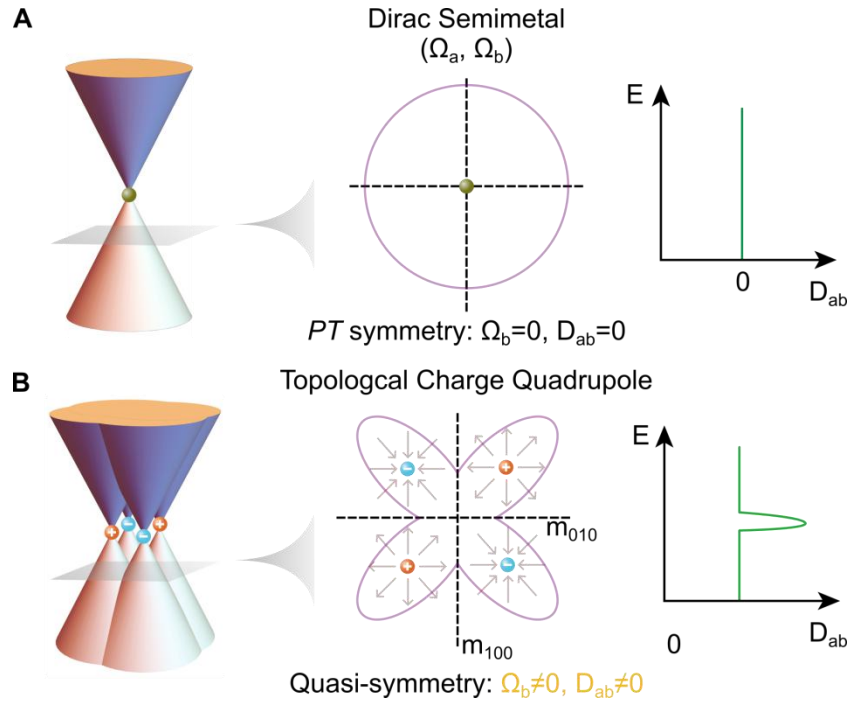


**Fig. 1. Schematics of the Dirac fermion and the topological charge quadrupole (TCQ).** (A) A Dirac semimetal protected by  $PT$  symmetry exhibits zero Berry curvature ( $\Omega_b$ ) and zero Berry curvature dipole ( $D_{ab}$ ). (B) A topological charge quadrupole is protected by the quasi-symmetry, resulting in a significant Berry curvature and Berry curvature dipole. The orange and blue spheres represent Weyl points with the monopole charge +1 and -1, respectively. The medium panels in (A-B) represent Fermi surfaces and Berry curvatures of the Dirac cone and TCQ, respectively.

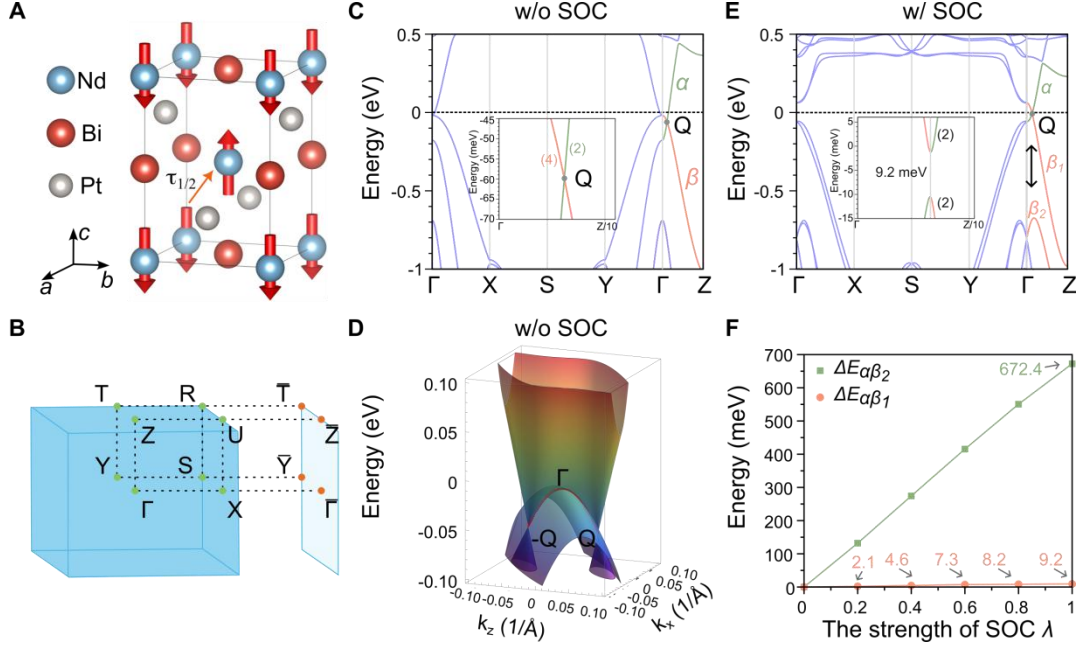


**Fig. 2. Magnetic structure and electronic structures of NdBiPt.** (A) The magnetic structure of collinear AFM NdBiPt. (B) Bulk and surface Brillouin zones (BZs) of NdBiPt. (C) The electronic structure of NdBiPt without spin-orbit coupling (SOC). The inset in (C) shows the degeneracy between  $\alpha$  and  $\beta$  bands. (D) Three-dimensional electronic structure of NdBiPt. The red line denotes the Dirac nodal line within the  $k_z - k_x$  plane without SOC. (E) The electronic structure of NdBiPt with SOC. The inset in (E) shows the tiny gap between  $\alpha$  and  $\beta_1$  bands. The green and orange bands denote the  $\alpha$  and  $\beta_1/\beta_2$  bands, respectively. The black arrow indicates the gap  $\Delta E_{\alpha\beta_2}$  between  $\alpha$  and  $\beta_2$  at the Q (0, 0, 0.006) point (fractional coordinates). The Fermi level is set to zero. (F) The band gaps  $\Delta E_{\alpha\beta_1}$  and  $\Delta E_{\alpha\beta_2}$  as a function of the spin-orbit coupling strength  $\lambda$ .

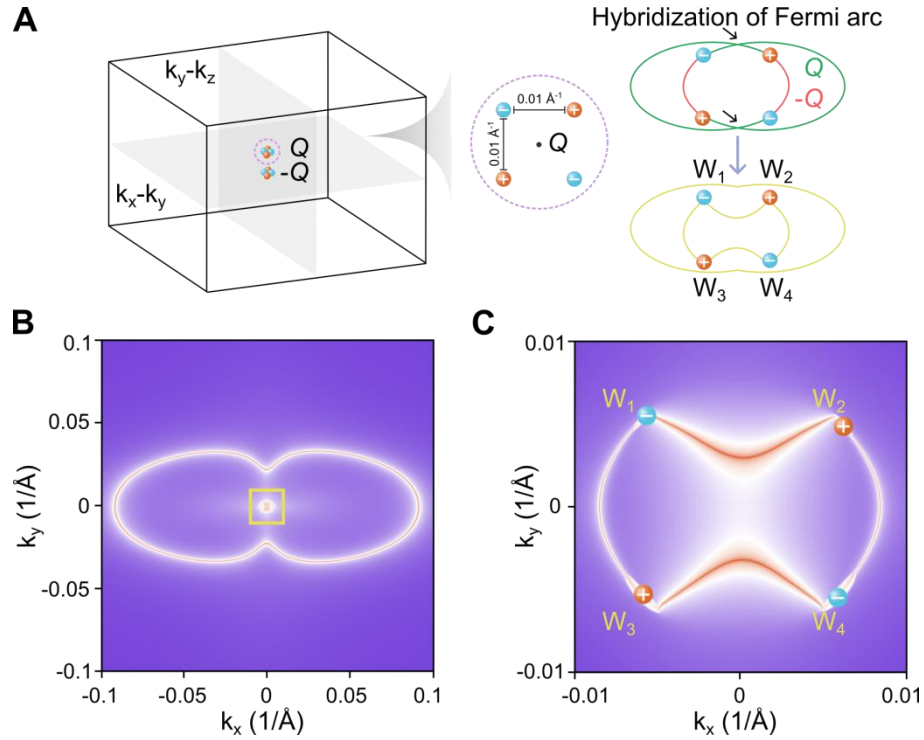


**Fig. 3. The distribution and Fermi arcs of TCQ.** (A) The distribution of topological charge quadrupole in the Brillouin zone of NdBiPt. The orange and blue spheres represent Weyl points with the monopole charge +1 and -1, respectively. The right panel of (A) shows a schematic diagram of two closed Fermi rings formed by the hybridization of Fermi arcs. The green and red lines represent the Fermi arcs located at  $Q$  and  $-Q$ , respectively. (B) The isoenergy surface states enclosing topological charge quadrupole on the  $k_x - k_y$  plane at 5.8 meV below the Fermi energy. (C) An enlarged view of the yellow square is marked in (B).

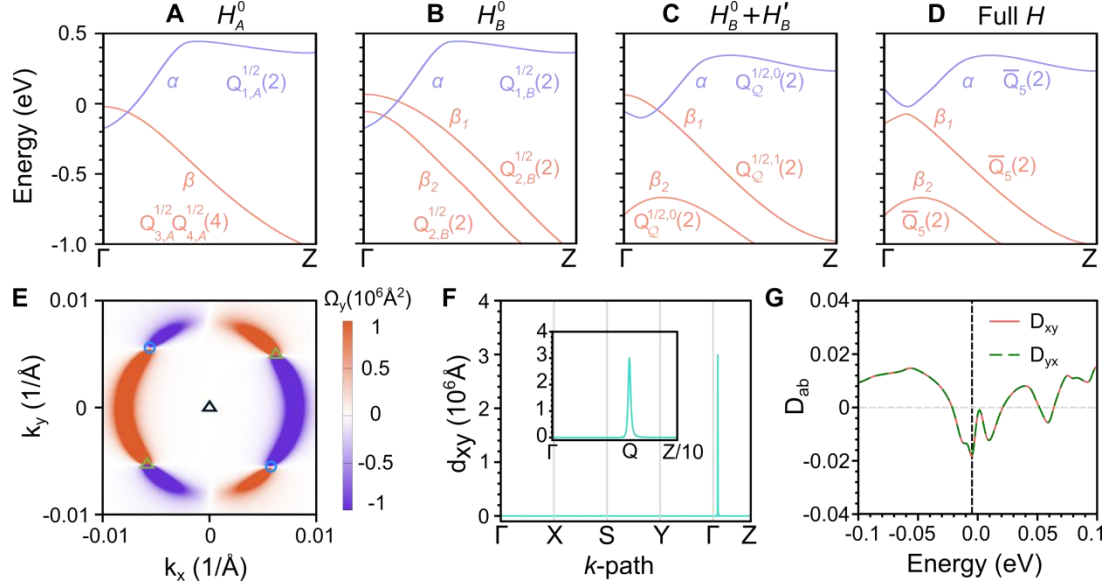


**Fig. 4. Quasi-symmetry and the nonlinear Hall effect in NdBiPt.** (A-D) Evolution of bands  $\alpha$  and  $\beta_1, \beta_2$  for NdBiPt when considering different Hamiltonians  $H_A^0, H_B^0, H_B^0 + H'_B$ , and the full Hamiltonian  $H$ , respectively. (E) Distribution of the Berry curvature within the  $k_x - k_y$  plane. (F) BCD density  $d_{xy}$  along the high-symmetry line. The inset in (F) denotes  $d_{xy}$  along the  $\Gamma - Z/10$ . (G) Berry curvature dipole  $D_{ab}$  as a function of energy. The black dashed line represents the energy position of the  $Q$  point, which is 5.8 meV below the Fermi energy.